Anatomy of a Strombolian eruption: Inferences from particle data recorded with thermal video

Maxime Bombrun, Andrew Harris, Lucia Gurioli, Jean Battaglia, Vincent Barra

AGU PUBLICATIONS

JGR

Journal of Geophysical Research: Solid Earth

RESEARCH ARTICLE
10.1002/2014JB011556

Key Points:
- Strombolian ballistics are geophysically defined
- A database of 83,000 particles is provided
- These parameters allow a better understanding of plume dynamics

Correspondence to:
M. Bombrun,
bombrun@isima.fr

Citation:
Bombrun, M., A. Harris, L. Gurioli, J. Battaglia, and V. Barra (2015), Anatomy of a Strombolian eruption: Inferences from particle data recorded with thermal video, *J. Geophys. Res. Solid Earth*, *120*, 2367–2387, doi:10.1002/2014JB011556.

Received 22 AUG 2014
Accepted 2 MAR 2015
Accepted article online 6 MAR 2015
Published online 28 APR 2015
Corrected 25 MAY 2015

This article was corrected on 25 MAY 2015. See the end of the full text for details.

Anatomy of a Strombolian eruption: Inferences from particle data recorded with thermal video

Maxime Bombrun[1,2,3,4], Andrew Harris[1,2], Lucia Gurioli[1,2], Jean Battaglia[1,2], and Vincent Barra[3,4]

[1]Clermont-Université, Université Blaise Pascal, LMV, Clermont-Ferrand, France, [2]CNRS, UMR 6524, LMV, Aubiere, France, [3]Clermont-Université, Université Blaise Pascal, LIMOS, Clermont-Ferrand, France, [4]CNRS, UMR 6158, LIMOS, Aubiere, France

Abstract Over the past decade, a proliferation of new technologies has pushed forward our ability to measure the dynamics of volcanic emissions as they exit, and ascend above, the vent. Measuring parameters of all particles as they exit the vent during an explosive eruption is the best way to gather parameters such as size, shape, velocity, and mass for the solid (particulate) fraction of the plume, in our case this being the lapilli and bomb component. We compute particle velocities and size distributions using high spatial resolution (centimeter-sized pixel) thermal infrared imagery collected at 200 Hz for small explosive eruptions at Stromboli (Italy). Our study covers 13 eruptions from Stromboli's southwest crater that occured in October 2012, plus 13 eruptions from the southwest crater, and 5 eruptions from the northeast crater in May 2014. We obtain a statistically robust database for size, mass, and velocity of 83,000 particles. Most particles have sizes of 5 to 15 cm so that the majority of individual particle masses are below 0.4 kg. However, 4950 (6%) of the particles are heavier than 5 kg and represent 59% of the total mass erupted. We also show that the smallest particles detected have the highest velocities with the maximum recorded vent-leaving velocity being 240 m/s. While the thermal data provide insights into particle emission and launch dynamics, correlation with seismic data sheds light on the source mechanism. Our results lead us to suggest that pyroclast-dominated explosions are a consequence of the presence of a viscous, degassed cap at the head of the magma column, whereas gas-dominated events are a consequence of slug bursting in a "cleaner" conduit, the cap having been lost by convective overturn.

1. Introduction

Emission of bombs, blocks, lapilli, and minor coarse ash is common during normal explosive activity at Stromboli volcano (Aeolian Islands, Italy). In addition, eruptions occur (on average) 13 times an hour and are sufficiently small that measurements can be made, and methodologies tested, close to the source in reasonable safety [*Harris and Ripepe*, 2007; *Ripepe et al.*, 2008]. Stromboli has thus become famous as being an outstanding natural laboratory for studying the source and dynamics of explosive emissions. Because measurement of particle exit parameters is an important objective in the study of explosive emissions, studies aimed at designing methodologies to extract parameters, and to create particle size, mass, and velocity databases, have tended to target Stromboli [*Chouet et al.*, 1974; *Ripepe et al.*, 1993; *Patrick et al.*, 2007; *Delle Donne and Ripepe*, 2012; *Harris et al.*, 2012, 2013; *Taddeucci et al.*, 2012a]. Recently, technological advances, including the development of field-portable high-speed visible and thermal cameras, have allowed new insights into particle emission dynamics and how those dynamics relate to associated source processes [*Patrick et al.*, 2007; *Taddeucci et al.*, 2012a; *Harris et al.*, 2012; *Gurioli et al.*, 2013, 2014; *Genco et al.*, 2014]. However, despite the frequency of activity and number of particles involved in each emission at Stromboli, large, statistically robust databases for vent-leaving particle dynamics remain scarce.

Particle size distribution has long been known to be a particularly useful parameter to measure if we are to understand the fragmentation process and particle emission dynamics [e.g., *Walker*, 1971, 1973; *Wohletz et al.*, 1989]. These data can be obtained from the deposit or from visible and infrared imagery of an active eruption [e.g., *Chouet et al.*, 1974; *Ripepe et al.*, 1993; *Harris et al.*, 2012]. Likewise, individual particle and total deposit mass has increasingly been obtained from thermal camera imagery [*Patrick et al.*, 2007; *Taddeucci et al.*, 2012b; *Harris et al.*, 2013; *Delle Donne and Ripepe*, 2012]. Mass and mass flux are again fundamental parameters for understanding the dynamic evolution of an explosive event, as well as for event classification and characterization in terms of magnitude and intensity [*Newhall and Self*, 1982]. Emission, or launch, velocity is a key parameter for constraining particle trajectories and fall out range [e.g., *Lorenz*, 1970; *Self et al.*, 1980; *Kilgour et al.*, 2010]. Initially, particle velocities were obtained using photoballistic analysis of visible imagery

[*Chouet et al.*, 1974; *Blackburn et al.*, 1976; *Ripepe et al.*, 1993], but thermal camera imagery is becoming increasingly used [*Patrick et al.*, 2007; *Harris et al.*, 2012; *Delle Donne and Ripepe*, 2012] along with videos from high-speed visible cameras [*Taddeucci et al.*, 2012a; *Gaudin et al.*, 2014a, 2014b; *Genco et al.*, 2014].

The use of portable (handheld) forward looking infrared (FLIR) cameras has become widespread in volcanology since their first use by *McGimsey et al.* [1999] to image warm deposits at Pavlof and Shishaldin volcanoes between 1997 and 1999 [*Harris*, 2013]. Thermal infrared imagery collected at wavelengths of 7–14 μm is able to achieve a number of tasks difficult or impossible to accomplish using other tools. The main advantage offered by the infrared camera is that the hot particles are easily spotted due to their high contrast when set against a cool background. In addition, small (subpixel) hot particles, invisible to the naked eye, become apparent due to their lighting up of a whole pixel [*Harris et al.*, 2012].

Here we use thermal video data to fully parameterize the emission dynamics of bombs, blocks, and lapilli as they leave the vent. Following emission, these will typically follow ballistic trajectories [e.g., *Vanderkluysen et al.*, 2012], unlike the plume of gas and fine particles whose ascent will be buoyancy driven [e.g., *Turner*, 1962]. For the lapilli through bomb size range, we present a large database of particle sizes, velocities, masses, shapes, kinetic energies, and number. Because of our frame rate (200 Hz), this allows generation of frequency distributions with thousands of points for each eruption, even if the emission lasts just a few seconds. We use these results to further develop the source mechanism and emission model for ballistic-dominated explosive events at Stromboli proposed by *Gurioli et al.* [2014].

2. Methodology

The thermal camera used in this study was a forward looking infrared (FLIR) manufactured by FLIR Systems, it being the SC655 which acquires a 640 × 480 pixel image at wavelengths of 7–14 μm. The camera was equipped with a 3.6X magnification lens and recorded at 200 frames per second. To allow data transfer at these frame rates, the image height must be reduced to 120 pixels. The lens focal length (f) was 88.9 mm and the pixel spatial resolution (or instantaneous field of view, IFOV) was 0.19 mrad. For this study, images were acquired from a location that was higher than the target so that the line of sight was oblique. The average distance between the camera and the eruption plane was around 280 m. Following *Holst* [2000], at this distance (d), we should be able to detect particles with diameter (D) down to

$$\begin{aligned} D &= d \times \mathrm{IFOV} \\ &= 280 \times 1.9 \times 10^{-4} \\ &= 5.3\ \mathrm{cm} \end{aligned} \tag{1}$$

To extract quantitative information for each particle, we need to convert the pixel dimensions (X_{pix}, where X is the pixel width or height) into millimeters (X_{mm}). This is calculated by

$$X_{mm} = YX_{pix} \tag{2}$$

in which Y is a scaling factor given by

$$Y = \frac{Rd}{f \sin(90 - \phi)} \tag{3}$$

in which R is the spatial resolution of the camera described as a ratio of the pixel IFOV to the image field of view and ϕ is the tilt angle of the camera during the acquisition.

Unless we apply a pixel mixture model to understand the size of a hot subpixel particle [e.g., *Harris et al.*, 2012], the limit of our measurement will be 1 pixel, i.e., 5.3 cm at our distance. Particles smaller than the pixel size will be missed or, if they are large enough and hot enough to light up the pixel, lumped into the 5.3 cm size bin. Thus, we just consider the lapilli and bomb component of the emission, i.e., all particles with a diameter greater than 5.3 cm. However, following *Gurioli et al.* [2013], for such eruption types, this size range accounts for more than 50% of the solid fraction of the emission by mass. The 2-D image allows us to estimate dimension only in the image plane, so we have to assume symmetry to obtain 3-D information. Some ejecta will be moving toward or away from the camera, thus changing their apparent size in terms of pixel dimension as they move. These issues can be solved with stereoscopic imaging, but our method is specifically designed for cases where stereoscopic measurements are either impractical or unavailable. We note, though,

that given the high frame rate and magnification of our video, such effects will be absolutely minimal. In effect, the magnification lens allows us to focus on a window just above the vent so that the particles will still be close to their emission point; i.e., they will be moving more or less vertically out of the vent. Besides, there is typically very little difference in their position between two frames due to the high frame rate (1/200th of a second); so there is little effect due to movement toward or away from the focal plane.

2.1. Target

Stromboli volcano (Aeolian Islands, Italy) was selected as a target, it being a reliable emitter of particles where weakly explosive activity has persisted at least since 500 A.D. [*Rosi et al.*, 2000]. We completed two measurement campaigns, one in 2012 and a second in 2014. In 2012, we completed 8 h of recording spread over 4 days spanning 27 September to 5 October 2012, during which time we recorded 13 eruptions. In 2014, we recorded for 8 h on 17 and 18 May, capturing a further 18 events.

We set up the thermal camera at Pizzo Sopra la Fossa (PSF: 918 m above sea level) which overlooks Stromboli's active crater terrace. The terrace itself is aligned NE-SW with dimensions of 200 by 230 m and contains all of the active vents. In historical times, the crater terrace has hosted three main craters [*Washington*, 1917], which today are named southwest (SWC), central (CC), and northeast (NEC). During 2012, SWC hosted two active vents, two puffing vents were active atop a small cone in CC, and NEC also contained two active vents. In 2014, SWC contained three active vents, plus four degassing vents. CC comprised a large central cone, whose summit vent produced near continuous spattering and explosions, and NEC comprised two pits each containing an active vent. We set up on the SW end of PSF (universal transverse Mercator (UTM) coordinates: WGS84 0518574 4293754) from where we viewed the most active vent in SWC over a line of sight distance of 280 m. We also set up on the NE end of PSF (UTM coordinates: WGS84 0518580 4293785) from where we were also able to record data for an active vent in NEC over a distance of 250 m. All 13 eruptions recorded during 2012 were from SWC, with 13 eruptions being recorded from SWC in 2014 and five from NEC. Each event is referenced using four digits for the month and day (MM-DD) then nine digits for the time (in hour, minutes, seconds, and nanoseconds) from the beginning of the video clip from which the data sequence is extracted (HHMMSSNNN). During the 2012 campaign, a Guralp CMG-40 T 30 s broadband seismometer was also installed near the thermal camera acquisition point.

In this study, we are not interested in trajectories. Instead, our aim is to capture the vent-leaving properties of all measurable particles, primarily size, velocity, shape, and mass. This measurement location places us as close to the point of fragmentation as possible. Such parameters collected later along the flight path, or once the particle is on the ground, will be very different and heavily modified as compared with those that were actually present as the particles exited the vent. For example, a molten fragment may deform and break-up in-flight as well as upon ground impact. This will change the field collected shape and size parameters. Thus, by computing particle parameters as soon as they exit the vent, our results are valid for the vent-leaving conditions. Consequently, we focus on single frame analysis using the closest usable frame to the vent.

2.2. Parameter Extraction

Given (i) the large number of particles (tens of thousands), (ii) high particle velocities (hundreds of meters per second), and (iii) the quantity of data (two hundred 640×120 pixel images per second = 150 kb/s in size or 1.8 Gb/min), we need a simple and efficient algorithm to allow parameter extraction. Here we used an algorithm based on a mathematical morphology transformation hybridized by thresholding [*Bombrun et al.*, 2014]. This algorithm allowed us to identify and count most of the particles as they exited the vent in cases where plumes of finer particles did not obscure the bombs and lapilli we track.

To characterize particle dimension, we considered the radius of the short-axis (r_S) and the radius of the long-axis (r_L). Using these measurements, we defined the characteristic radius (r) using the two axes, so that $r = (r_S + r_L)/2$. To convert to particle volume, we applied a spheroidal assumption that used the short- and long-axis radii to estimate the volume of particle i (V_i). Particles that are fluid and, at the vent, moving at high velocity in a quasi-vertical direction tend to take on an elongate shape stretched in the direction of flight [*Macdonald*, 1972]. This can be best described by a prolate spheroid, so that

$$V_i = \frac{4}{3}\pi r_S^2 r_L \tag{4}$$

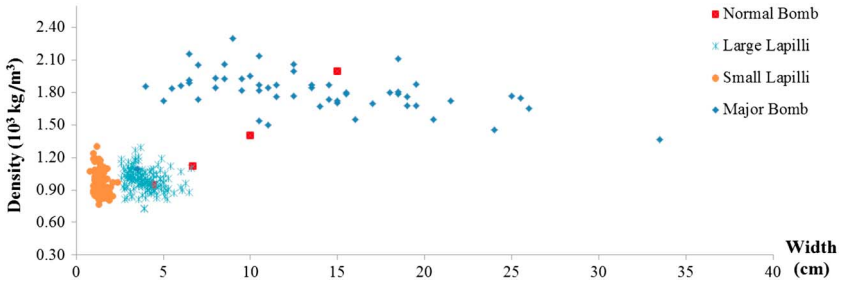

Figure 1. Density of lapilli and bombs measured from samples of Stromboli's scoria collected between 2008 and 2011.

Now given an appropriate density (ρ_i), particle volume can be converted to mass (m_i):

$$m_i = \rho_i V_i \tag{5}$$

To define an appropriate density, we plotted density versus *b* axis length for lapilli and bombs collected at Stromboli between 2008 and 2011 (Figure 1). This plot combined measurements from samples of fine (1–2 cm) and large (4–5 cm) lapilli collected during June 2008 from two bomb-dominated normal explosions [*Colò*, 2012] plus 53 bombs taken from a bomb field from a major explosion of January 2010 by *Gurioli et al.* [2013]. We also plotted the density of two bombs collected in 2008 [*Gurioli et al.*, 2014], from a bomb-dominated normal explosion whose particle trajectories were defined by *Vanderkluysen et al.* [2012] plus two bombs collected from a gas-dominated explosion in 2011 [*Leduc et al.*, 2015]. For the density conversion, we split the distribution into two fields: lapilli and bombs. For bombs (6.5 cm to 35 cm), we see no trend with increasing size, but the cluster is fairly tight with a mean and standard deviation of 1 800 ± 200 kg/m^3. Likewise, the lapilli (0.2 cm to 6.5 cm) form a cluster with a mean and standard deviation of 980 ± 110 kg/m^3. We use these two values for our size-dependent conversion to mass. Thus, the mass of all particles detected is calculated with an error ±11% due to the uncertainty in density.

The tracking step of the algorithm computed the velocity of particles following first detection [*Bombrun et al.*, 2014]. In raw form, this is expressed in terms of the number of pixels travelled by the particle between two consecutive frames separated by time *t*. This will be in units of pixels per frame. Thus, the pixel velocity (*U*) of the particle *i* at time *t* is

$$U_{i,t} = \frac{\left\|\omega_{i,t+1} - \omega_{i,t}\right\|}{(t+1) - t} \tag{6}$$

where $\omega_{i,t}$ is the position of the particle *i* at time *t*. We now complete the transition to velocity in m/s using

$$U_{[\mathrm{m/s}]} = \nu Y \times U_{[\mathrm{pix/fr}]} \times 10^{-3} \tag{7}$$

in which ν is the frequency of image acquisition and *Y* is the scale factor defined in equation (3).

Particle locations are accurate to within 1 pixel, leading to absolute uncertainties on velocity of ±0.2 m/s (for particles traveling vertically) which can lead to an uncertainty of ±2 m/s in the worst case of a particle moving away from the focal plane at an angle of 6°. Now, given particle velocity (U_i) and mass (m_i), we can estimate the particle kinetic energy (ε_i):

$$\varepsilon_i = \frac{1}{2} m_i U_i^2 \tag{8}$$

The particle database for each eruption can now be used to produce particle size, mass, and velocity distributions. We can thus produce distributions for each parameter and integrate each parameter through time to obtain volumes, masses, and energies released over given periods of time. To do this, let $K = \{m, V, \varepsilon\}$, so that

$$K_t = \sum_i \mathrm{K}_i \tag{9}$$

where K_t is the global parameter $\{V, m, \varepsilon\}$ for all particles. If integrated over the entire emission, this will yield total volume, mass, or kinetic energy. If integrated over discrete time steps, and divided by time step duration, this will give volume or mass flux.

Table 1. Comparison of Data for a Single Explosion From 2012, All SWC Explosions From 2012, All SWC Explosions From 2014, and All NEC Explosions From 2014

Parameter	Set	Minimum	Maximum	Mean	Standard Deviation	Skew	Kurtosis
Width (cm)	09-30_135413067	5.5	37	11	4.0	1.7	4.4
	SWC 2012	5.5	64	12	5.5	2.2	7.8
	SWC 2014	5.7	73	7.8	5.0	4.4	27
	NEC 2014	6.1	64	9.3	5.3	3.1	14
Mass (kg)	09-30_135413067	$0.2 \pm 1.7 \times 10^{-2}$	32 ± 4	1.2 ± 0.1	2.2 ± 0.2	6.2	53
	SWC 2012	$0.2 \pm 1.7 \times 10^{-2}$	214 ± 24	2.3 ± 0.3	6.2 ± 0.7	12	230
	SWC 2014	$0.2 \pm 1.9 \times 10^{-2}$	287 ± 32	1.2 ± 0.1	6.9 ± 0.8	16	385
	NEC 2014	$0.2 \pm 2.4 \times 10^{-2}$	223 ± 25	1.6 ± 0.2	6.3 ± 0.7	14	307
Velocity (m/s)	09-30_135413067	8.2	216	34	23	2.9	12
	SWC 2012	7.7	224	33	24	3.1	13
	SWC 2014	8.0	226	51	39	1.5	2.1
	NEC 2014	8.6	240	53	39	1.8	3.0
Average total kinetic energy (MJ)	09-30_135413067			4.1			
	SWC 2012			3.9			
	SWC 2014			4.4			
	NEC 2014			11			
Average number of particles detected per second	09-30_135413067			260			
	SWC 2012			156			
	SWC 2014			202			
	NEC 2014			451			
Total number of particles detected	09-30_135413067			5,449			
	SWC 2012			29,552			
	SWC 2014			31,493			
	NEC 2014			22,175			

2.3. Classification

To classify the eruption type, we used histograms for velocity, size, and mass for each explosion. For velocity and size we used 11 bins, and 26 bins for mass, which when lumped together provided a total of 48 dimensions available for event characterization. We used the *k*-means algorithm of *MacQueen* [1967], this being an iterative refinement technique which partitions observations into *k* clusters by minimizing the distance between the observation and the centroid of a cluster. Usually, the Euclidean distance is used for clustering [e.g., *MacQueen*, 1967]. However, we used the Bhattacharyya distance [*Bhattacharyya*, 1943] which, rather than a measure of spatial similarity, is a measure of the similarity of two probability distributions, as is appropriate for the case in hand.

3. Results

We begin by considering a single eruption from the southwest crater in 2012. The eruption occurred on 30 October at 11:58:26 UTC (reference: 09-30_135413067). The eruption lasted 17 s during which 4382 particles were detected, meaning that, when time averaged, the emission rate was 258 particles per second. The particle size distribution has a peak at the interval of 8 cm to 10 cm, with a mean particle width of 11 cm and a standard deviation of 4 cm, indicating a slight skew toward larger particles. Such a positive skew is common to all distributions (see Table 1). The particle mass distribution revealed that most particles had a low mass, where 3773 or 86%, of all of the detected particles had a mass of less than 2 kg. This population accounts for 2470 kg, or 45%, of the total mass. The remaining 1912 or 14% of the particles thus accounted for 55% of the total mass ejected, this being 5450 kg.

The velocity distribution had a mode between 20 m/s and 30 m/s, with an average velocity of 34 m/s on which the standard deviation was 23 m/s. Particle velocities at Stromboli are generally less than 100 m/s [*Chouet et al.*, 1974; *Blackburn et al.*, 1976; *Ripepe et al.*, 1993; *Patrick et al.*, 2007]. Here 97.6% of all of particles measured had velocities of less than 100 m/s. However, 103 particles (2.3%) had velocities greater than 100 m/s, and up to 216 m/s. This approaches the higher velocities recently found for normal explosive activity at Stromboli by *Taddeucci et al.* [2012a], *Delle Donne and Ripepe* [2012], *Harris et al.* [2012], and *Genco et al.* [2014]. All of our fast moving particles are relatively small, being less than 20 cm in width. The kinetic energy

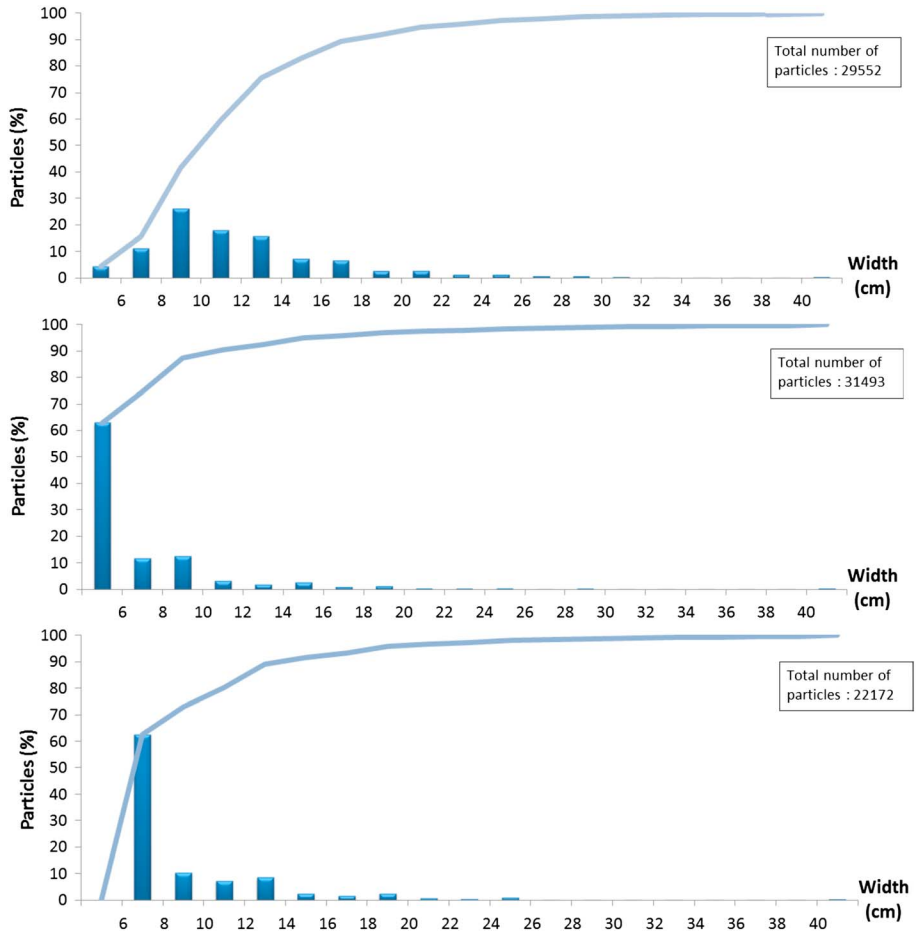

Figure 2. Particle size distribution for eruptions from (a) SWC in 2012, (b) SWC in 2014, and (c) NEC in 2014 with the cumulative number of particles detected for each case.

carried by lapilli and bombs during this eruption was 4.1 MJ, the equivalent of 1 kg of TNT. This is consistent with the kinetic energy range of 0.7 to 5.2 MJ as measured at Stromboli during four explosions by *Ripepe* [1996] in 1991. These similarities down the years point to a consistency in the intensity and magnitude of activity over the time scale of decades and to the temporal resilience of the system.

3.1. The 2012 Data Set

While overview statistics for all eruptions recorded during the 2012 campaign are given in Table 1, the statistics for each of the 13 eruptions recorded in 2012 are given in Appendix A. Emission durations ranged from 5 s to 50 s, with an average of 16 s. The number of particles detected during a single explosion ranged from 650 to 5240, with an average of 2270. A total of 29,550 particles were detected during all 13 eruptions. Statistically, the distribution for all parameters derived from the total 2012 data set was similar to that obtained for the single eruption described above. We thus assume that all events were analogous or self-similar and thus can be related to the same process. From here onward, we thus consider the total data set as a reliable descriptor of all 2012 events studied by us.

Due to the large number of particles detected, the data set is statistically robust; even if some false detections occurred, they will have a vanishingly small impact on the final statistics. The particle size distribution (Figure 2a) reveals that the majority of the particles (82%) had widths of between 5 cm and 15 cm with an average of 12 cm. However, these results have to be treated with caution because particles with widths less than 5 cm will not be detected due to the spatial resolution of our system. Masses erupted range between 1270 kg and 11,820 kg, with an average of 5340 kg. Individual bombs have masses of up to 214 kg, and while 90% of the particles were less than 5 kg, 75% were less than 2 kg (Figure 3a). However, the 1021 particles greater than 25 cm (i.e., 3.4% of the total detected particles) account for 36% of the total mass. Velocities again had a mode between 20 m/s and

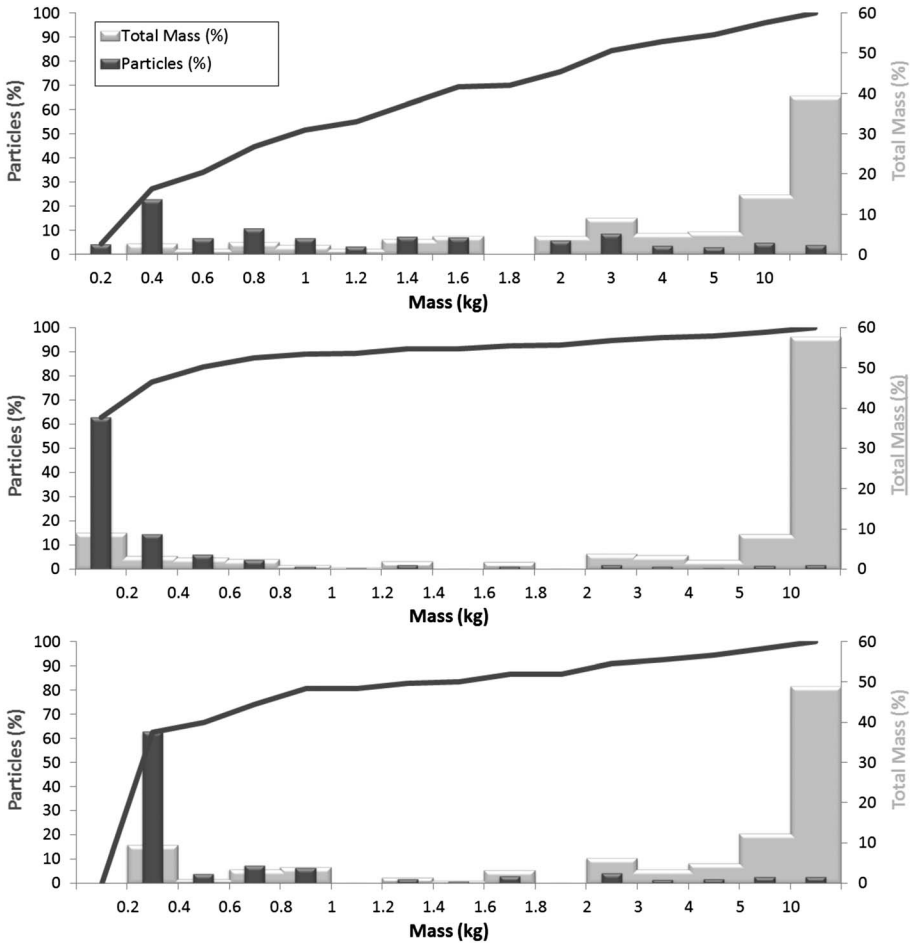

Figure 3. Particle mass distribution, total mass distribution, and distribution function for eruptions from (a) SWC in 2012, (b) SWC in 2014, and (c) NEC in 2014. The light gray histogram shows the impact of heavy particles on the total mass ejected.

30 m/s with an average of 33 m/s (Figure 4a), and 97% of particles had a velocity less than 100 m/s, with the maximum velocity being up to 224 m/s.

3.2. The SWC Data Set From 2014

First, we focus on the 13 eruptions which occurred from the southwest crater. This data set provides information on a further 31,500 particles. These statistics are summarized in Table 1 and broken down by eruption in Appendix B1. Emission durations ranged from 6 s to 22 s, with an average of 12 s, and the number of particles detected during a single explosion ranged from 610 to 4385, with an average of 2420. A total of 31,500 particles were detected during all 13 eruptions. The particle size distribution (Figure 2b) reveals that the majority of the particles (63%) were below 6 cm and the distribution was tighter than in 2012. Masses erupted ranged between 1840 kg and 4740 kg, with an average of 2908 kg. Ninety-six percent of the particles were less than 5 kg, and 93% were less than 2 kg (Figure 3b). However, the 584 particles that were greater than 25 cm (i.e., 1.8% of the total detected particles) accounted for 56% of the total mass. The particle velocity distribution (Figure 4b) had a mode between 20 m/s and 30 m/s. The average was 51 m/s, with 88% of the particles having a velocity of less than 100 m/s, the maximum velocity being 226 m/s.

3.3. The NEC Data Set From 2014

Now we consider the five eruptions which occurred at the northeast crater in 2014. This data set provides information for a further 22,175 particles. These statistics are summarized in Table 1 and are broken down by eruption in Appendix B2. Emission durations ranged from 7.5 s to 16 s, with an average of 10 s. The number of particles detected during a single explosion ranged from 2580 to 5320, with an average of 4435. A total of 22,175

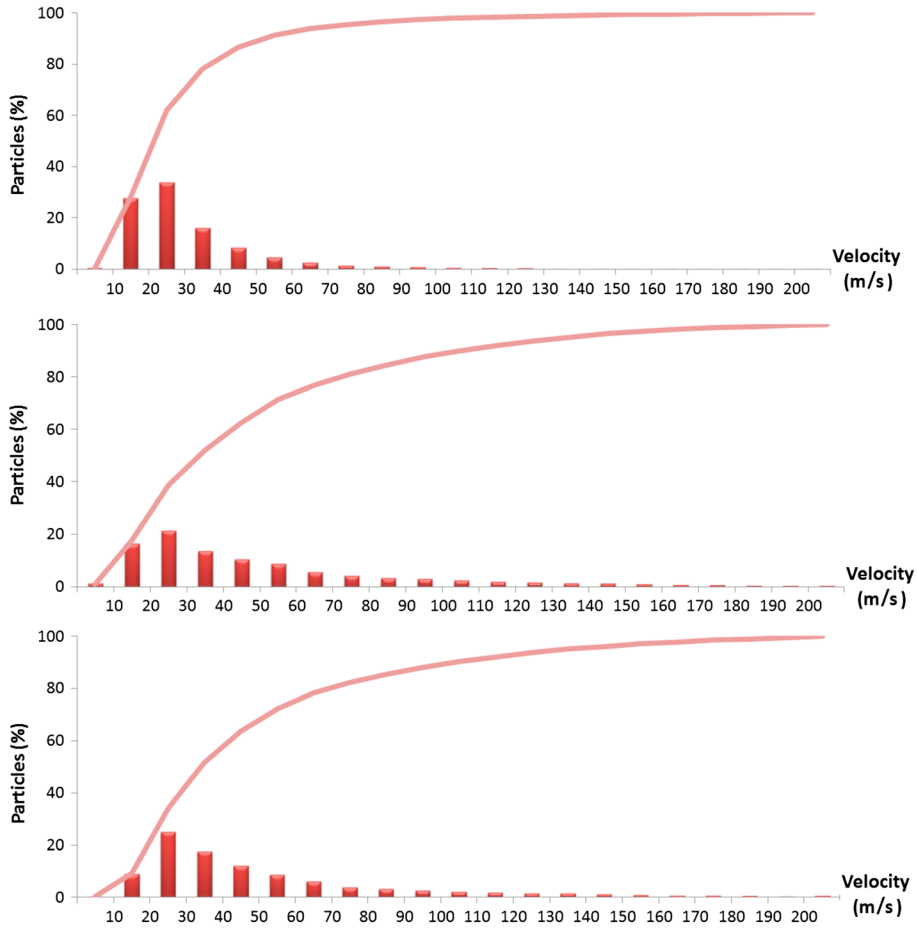

Figure 4. Particle velocity distribution and distribution function for eruptions from (a) SWC in 2012, (b) SWC in 2014, and (c) NEC in 2014.

particles were detected during all five eruptions. We note that emission rates in terms of the number of particles per second (pps) was higher at NEC (450 pps) than at SWC during both 2012 (155 pps) and 2014 (200 pps). The particle size distribution for NEC (Figure 2c) was similar to that of the SWC with a mode between 6 cm and 8 cm. Masses recorded at NEC ranged between 3540 kg and 10,255 kg with an average of 6845 kg. Ninety-five percent of all particles erupted were less than 5 kg, and 87% were less than 2 kg (Figure 3c). However, the 495 particles that were greater than 25 cm (i.e., 2.2% of all detected particles) accounted for 45% of the total mass. The velocity distribution (Figure 4c) had a mode between 20 m/s and 30 m/s, with an average of 52 m/s. For the NEC case, 88% of particles had a velocity less than 100 m/s, with the maximum velocity being 240 m/s.

3.4. Differences: 2012 Versus 2014—A Measure of Fragmentation Efficiency?

The proportion of low mass particles erupted in 2012 (75% $<$ 2 kg) was less than in 2014 (93% $<$ 2 kg at SWC and 87% at NEC). This difference is reflected in the size distributions that were skewed toward bombs in 2012 and toward lapilli in 2014. Because bombs account for a disproportionate percentage of the mass of each eruption, the bomb-dominated SWC eruptions of 2012 were generally of a higher mass (average of 5340 kg) than in 2014 (average of 2908 kg) even though particles were erupted at a lower rate in 2012 (155 pps in 2012 versus 200 pps in 2014). This is all consistent with greater degrees of fragmentation, higher efficiency of fragmentation, and higher explosion energies in 2014 as opposed to 2012 so as to create a larger number of smaller particles in the second year. Indeed, kinetic energies were also higher at SWC in 2014 (average = 4.4 MJ) than in 2012 (average = 3.9 MJ). In addition, eruptions in 2012 had lower average velocities (33 m/s in 2012 versus 51 m/s in 2014) and a lower number of high-velocity particles; i.e., 3% were ejected at velocities greater than 100 m/s in 2012 compared with 12% in 2014. This seems to support the model where small particles are carried by the fast moving gas phase [*Harris et al.*, 2013], where the greater number of small particles

Table 2. Preliminary Results of the Clustering Algorithm on the 2012 Data Set[a,b]

Eruption Reference	Type 2a	Type 2b	Type 1	Type 2a + 1
09-27_154909271		KV		
09-27_155839983		KV		
09-28_135432903	KV			KV
09-30_125847157	K		V	KV
09-30_131721017			KV	KV
09-30_132029052			KV	KV
09-30_133102430_1			KV	KV
09-30_133102430_2	K		V	KV
09-30_134451828	K		V	KV
09-30_135413067	K		V	KV
10-05_144505552	V	K		V
10-05_145321701		KV		
10-05_150241747		KV		

[a]The visual clustering is represented by the V, whereas the *k*-means clustering is the K.
[b]Classification is between three types: ash with bombs and lapilli (Type 2a), ash without lapilli, and bombs (Type 2b) and gas-dominated plus coarse (Type 1).

available for gas transport in 2014 meant that there was a larger population of high-velocity particles in that year. These results point to a scenario, whereby changing degrees of fragmentation efficiencies can be tracked using the global mass and kinetic energy parameters, as well as the typical particle velocity, size, and number statistics for each eruption.

3.5. Classification

Patrick et al. [2007] classified normal explosions at Stromboli into two groups: Type 1 eruptions, which are dominated by coarse ballistic particles, and Type 2 eruptions, which are ash dominated with (2a) or without (2b) large number of lapilli- to bomb-sized pyroclasts. To this, *Leduc et al.* [2015] added a third category: Type 0. This event type is characterized by gas-dominated, high-velocity jets with velocities of hundreds of meters per second but involving few or no lapilli or bombs. *Goto et al.* [2014] geophysically defined such gas-rich and fragment-poor event types finding them to be characterized by a dominant shock wave component and supersonic velocities. Although *Goto et al.* [2014] termed this eruption style Type 3, we prefer Type 0 because this nomenclature fits the initial classification philosophy:

- Type 2: Two solid components = fine (ash) plus coarse (lapilli + bombs);
- Type 1: One solid component = coarse (lapilli + bombs);
- Type 0: No solid components = gas only (with aerosols);

Of course there is a continuum between these three classes of normal explosion. Type 0 may have a few or several particles entrained in the gas jet [*Leduc et al.*, 2015]; Type 2, as recognized by *Patrick et al.* [2007], may range between fine (Type 2a) and coarse (Type 2b) particle dominated. Likewise, Type 1 may be more or less particle loaded. All normal explosions will involve gas, but the key in this classification is the relative proportions of gas to fine and coarse material.

All parameters used to automatically classify the events are summarized in Table 1. These were used to separate the events into three classes, Types 2a, 2b, and 1 (we had no Type 0 cases), by running the clustering algorithm. We then completed a visual cluster analysis which classified the eruptions depending on their visual character as observed from viewing the thermal video. A comparison of the results from the automatic and manual methods is given in Table 2. We find that our algorithm separated out ballistic-dominated eruptions (Type 2b), misclassifying only one event. However, there is some mixing of Types 2a and 1. This is because the classification is based on particle parameters, and because Types 2a and 1 have been improved if we had simultaneous measurement of the fine particle and gas content. For now, if we lump Types 2a and 1 together, we only have one misclassification (Table 2).

3.6. Validation

In Figure 5, we compare our results (Figure 5b) with those obtained from 690 bombs sampled from a fall out field associated with a major (bomb dominated) explosion (Figure 5a) at Stromboli [*Gurioli et al.*, 2013]. We also compare our results with those obtained from a weak (lapilli dominated) explosion sampled toward the end of the 2012 campaign [*Harris et al.*, 2013]. This lapilli sampling involved laying out of four tarps (3×4 m plastic sheets) on 28 September 2012. These were placed on the outer flank of the SWC, 75 m SW of the active vent, and were retrieved in 5 October 2012. Upon retrieval, all juvenile coarse ash, lapilli, and Pele's hair were collected. This sample provides the "multiple-explosion" distribution of Figure 5c. On 5 October, fine material from SWC explosions was being blown (by the wind) off of the top of plume toward the SW. Here material

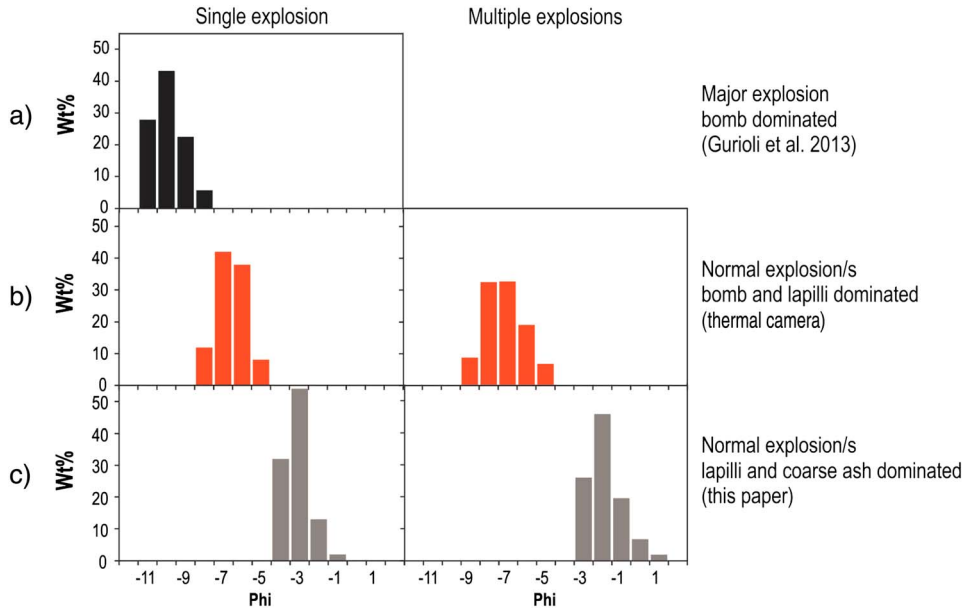

Figure 5. Particle weight percent by class size φ. For three eruption types: a (a) bomb-dominated explosion, a (b) normal explosions, and a (c) lapilli-dominated explosions.

landed on a tarp that had just been cleaned following an explosion at 15:50 (local time). Fall out onto the tarp began 20–30 s after bomb fall out within the crater was heard to finish and all coarse ash, lapilli, and Pele's hair that arrived during the 10 s long fall out event were collected. These were returned to the laboratory where their sizes and masses were measured. In total, 48 lapilli were collected for the 5 October 15:50 event with a total weight of 5.27×10^{-3} kg, the largest being 2.3 cm (6.8×10^{-4} kg) and the smallest being 2–3 mm (1.0×10^{-5} kg). This sample provides the "single-explosion" distribution of Figure 5c.

The thermal-camera-derived particle size distribution of Figure 5b is between the "bomb-dominated" and "lapilli-dominated" end-members and is similar to the distribution obtained by *Colò* [2012] for a normal explosion at Stromboli. We note that the fine tail made up of fine lapilli and coarse ash is not well defined because of the detection limits of our camera. In effect, particles smaller than the pixel size, i.e., 5.3 cm in diameter, are not detected. However, even if the number of particles that comprise the lapilli and ash component of such emissions is significant, their impact in terms of mass is not [*Gurioli et al.*, 2013].

The thermal-camera-derived particle size distribution shows a distribution between the bomb-dominated and lapilli-dominated end-members (Figure 5b). The lapilli-dominated samples collected from the tarps at SWC during the same campaign have a lapilli and coarse ash dominated distribution (Figure 5c). This is consistent with visual observations. On 27 September, SWC was noted as giving impressive bomb-rich and gas-rich explosions, with heavy bomb loading to 250 m above the vent, with NEC giving less frequent and less vigorous eruptions. However, by 5 October, the SWC was giving ash jets loaded with small bombs and lapilli, with the highest fragments reaching just 50 m above the vent. By this time, however, NEC was giving impressive bomb-rich bursts to 200–250 m. While most of the events sampled by the thermal camera were collected during the first 2 days of the 2012 sampling period (27 and 28 September), the sampling that contributes to the size distribution given in multiple-explosion distribution in Figure 5c was completed on 5 October and comprised fine-grained material that fell out on that day. Bad weather would have blown away all other material settling onto the sheets during the preceding days, and no bombs or burn holes were observed. This is supported by the agreement between the multiple-explosion and single-explosion distributions in Figure 5c.

For the single explosion sampled at 15:50 on 5 October, if we multiply the number of coarse ash, lapilli, and Pele's hair falling in our 12 m^2 control zone (areal number density = 4 m^{-2}) by the 4000 m^2 fall out area identified using the thermal imagery obtained from an airborne (helicopter) vantage point, we obtain a total particle number of 16×10^3 for this size range. This compares with a particle number of $1.3–1.6 \times 10^3$ for the coarse lapilli-bomb size range obtained for SWC eruptions using the thermal camera on the same day.

Table 3. Ballistic Exit Velocities for Eruptions at Stromboli and Etna[a]

Study		Velocity (m/s)			
Volcano	Method	Min	Max	Mean	Reference
Etna (Italy)	Photoballistics	15	79	51[b]	*McGetchin et al.* [1974]
Stromboli (Italy)	Photoballistics	2.5	72	26	*Chouet et al.* [1974]
Stromboli (Italy)	Particle tracking	-	-	22[c]	*Ripepe et al.* [1993]
Stromboli (Italy)	Thermal video (6 Hz)	26	71	47	*Vanderkluysen et al.* [2012]
Stromboli (Italy)	Thermal video (30 Hz)	3.0	101	34	*Patrick et al.* [2007]
Stromboli (Italy)	Thermal video (30 Hz)	9.0	129	46	*Harris et al.* [2012]
Stromboli (Italy)	Thermal video (50 Hz)	23	203	-	*Delle Donne and Ripepe* [2012]
Stromboli (Italy)	High-speed video (500 Hz)	<50	405	136	*Taddeucci et al.* [2012a]
Stromboli (Italy)	High-speed video (500 Hz)	0.1	241	51	*Gaudin et al.* [2014b]
Stromboli (Italy)	Thermal video (200 Hz)	7.7	240	45	This study
Mean $\overline{x}$ (standard deviation σ)		13 (10)	163 (123)	57 (40)	
Confidence interval[d]		3.0–23	40–286	17–97	

[a]Note that particles with diameters of 27 to 64 cm moving in the velocity range of 35–46 m/s are also reported in Figure 8a of *Ripepe et al.* [2001].
[b]Median value.
[c]Mean of the means from six eruptions with $\overline{x}$ of 16.3, 18.5, 15.8, 14.4, 22.3, and 21.7 m/s.
[d]The confidence interval is $[\overline{x} - \sigma - \overline{x} + \sigma]$. Data of *Ripepe et al.* [1993] and data of this study and minimum value from [*Taddeucci et al.*, 2012a] are not included.

However, if we multiply the mass area density for coarse ash, lapilli, and Pele's hair (0.44 g m^{-2}) by the fall out area, we obtain 1.8 kg, compared with 1270 to 11,822 kg obtained for the lapilli and bomb size range. Thus, for this lapilli-dominated event, while the thermal camera only captured 10% of the particles by number, it captured 100% of the emission by mass.

The last parameter we need to validate is the velocity of our particles. In *Bombrun et al.* [2014], we compared velocity obtained from our algorithm with that obtained by the algorithm of *Shindler et al.* [2012]. Comparison was completed on a synthetic data set of heated, falling ball bearings; the agreement was good. Furthermore, our results from Stromboli are consistent with ballistic particle velocities estimated using various other methodologies applied to image data for eruptions at Stromboli and Etna since 1974 (Table 3). The last row in Table 3 shows that the correlation between our results and those previous studies agrees within the 68% tolerance interval.

Uncertainty on our final level of measurement is a function of errors in particle shape and velocity, lack of constraint on the particle density, and errors due to omission and commission or false positives (missed particles and misidentified particles). The error on parameter computation is a function of pixel size, this being constrained by the sensor resolution, and camera distance from the target. False detections are hard to identify; however, the image environment at Stromboli is quite static so that errors of omission dominate over errors of commission. Using a controlled experiment, *Bombrun et al.* [2014] recovered 90% of particles released, with 95% of the size measurements being within the limit of agreement.

For measurements of lapilli and bomb-dominated explosions, our method thus appears valid and offers a means to obtain a larger database than is possible by field sampling. It can also provide data in real time multiple times a second. In addition, we measure the particle dimensions and shape at the vent, before modification due to in-flight tearing or collision, or fragmentation upon ground impact. To push the lower limit of our detection to smaller sizes, we could move the equipment closer to the source, or apply lenses with greater magnification, to the extent that safety and technology allows.

4. Discussion

Our method allows the construction of a data set containing size, mass, and velocity measurements for 83,000 particles emitted during 31 explosions. Similarity, between the parameters derived for the individual event used, the 2012 data set and the 2014 data set show that the events are extremely repeatable, suggesting that all types of eruption considered here (Types 2a, 2b, and 1) can be associated with a similar source mechanism which did not change within or between our measurement periods.

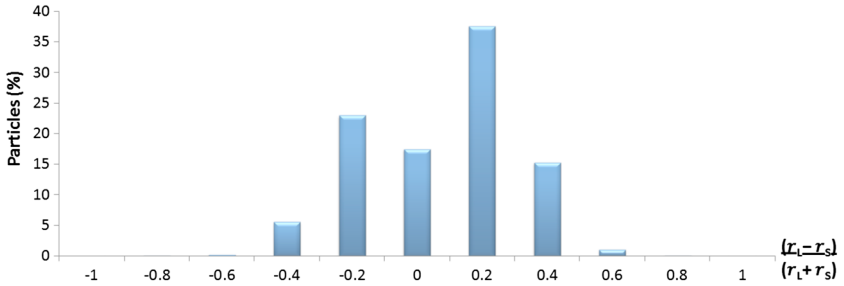

Figure 6. Particle shape distribution of the whole data set (SWC 2012 and SWC/NEC in 2014). Most of the particles do not have a spheroid shape but have either an oblate or prolate shape.

4.1. Particle Numbers, Sizes, Shapes, and Masses

Our particle counts range between 612 and 5316 per eruption, with an average of 2684 particles. In Figure 6, we assess particle shape in terms of the following normalized shape index: $(r_L - r_S)/(r_L + r_S)$. Using this index, a perfectly oblate shape will have a value of −0.3333, whereas a perfectly prolate shape will have a value of +0.3333; a perfect sphere will have a value of 0. We found that only 17% of our particles approximate a spherical shape. Of the remaining 83%, 29% are oblate and 54% are prolate. The dominance of the prolate shape is consistent with deformation or stretching in the direction of motion. Our prolate particles are up to 5.6 times longer (in the flight direction) than they are wide (index = 0.7). In the oblate direction, as we move from an index of −0.2 to −0.6, fragments become increasingly stringlike, being stretched in the horizontal direction until we reach a value of −1, which is technically impossible. On the video, fluid particles are seen to stretch in the flight direction, tear, and spin, with stretching occurring over time scales of tenths of a second. As already stated, our aim is to capture the initial vent-leaving shape before in-flight or ground impact-induced deformation and secondary fragmentation. We observe that both of these processes are beginning to occur, so as to modify the size and shape distributions, over just the first few meters of flight. However, we find no relation between size and shape, probably because all of our particles are quite large, molten, and deformable, so that all sizes in our range undergo motion-induced deformation.

The majority of *Chouet et al.*'s [1974] particles have diameters of less than 30 cm. In our study, 99% of the particles are below this limit, of which 62% fall in the bomb category (i.e., they are >6.4 cm). This reduces to 11.5% if we consider the absolute total from the projection of Figure 7. Our projections indicate that by size, the emission is dominated by particles smaller than 5.3 cm. This is consistent with the comparison with the lapilli field sample completed in 2012, where the thermal camera captured around 10% of the particles by number. In terms of total erupted masses during individual explosions, we obtain a range of 1270 to 11,822 kg, with a mean of 4585 kg. This is consistent with recent measurements of mass, which indicate eruptive masses of up to 35,000 kg [*Ripepe et al.*, 1993; *Ripepe*, 1996; *Harris et al.*, 2012], compared with 8 and 100 kg obtained by *Chouet et al.* [1974].

4.2. Projections and Correlations in the Total Data Set

If we plot size against the number of particles, we find that number increases with decreasing size in an exponential fashion (Figure 7). The trend indicates a total number of lapilli and bombs emitted during all 31 events of 450,000. Because we detect a total of 83,000 particles, due to spatial resolution problems, we are

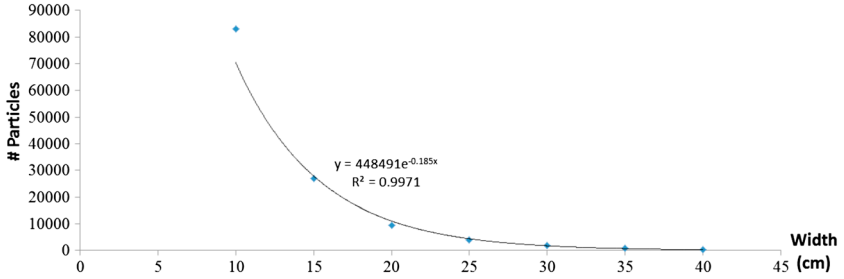

Figure 7. Trend between the total number of particles detected and their sizes.

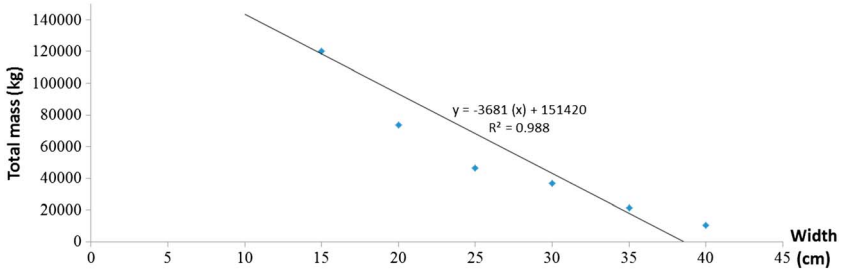

Figure 8. Trend between mass and width of particles.

missing around 367,000 of the smallest (<5.3 cm) particles. This leads us to underestimate the total particle number by 80%. The mass plot shows a linear relation between particle size and mass (Figure 8). The relation suggests the total mass erupted during the 31 events was 151,000 kg compared with the total mass measured of 142,000 kg. This means that we have captured at least 94% of the total mass emitted. This is consistent with the findings of *Gurioli et al.* [2013] who found that 31% of the mass erupted during a major explosive event at Stromboli was accounted for by the largest particles. In our case, most of the mass is accounted for by particles with a size greater than 5.3 cm. This means that even if we only detect 20% of the particles by number, we only underestimate the total mass by 6%, although both absolute totals (number of particles and mass) may be obtained from extrapolation of the two relations. This is again consistent with *Gurioli et al.* [2013] who found that although the largest particles (>1 m) accounted for 31% of the deposit by volume, such particles only accounted for 1% by number.

By number, the emission is thus dominated by small (<5 cm) particles. Currently, we can only obtain the small particle population by extrapolation from our limited, albeit statistically robust, data set. However, by mass, we can directly measure almost 95% of the emission. If we plot size against velocity, we find a degree of scatter. However, only the largest particles have the lowest velocities, and the smallest particles have the highest velocities (Figure 9). This is consistent with the results of *Harris et al.* [2012] who found that during explosions at Stromboli, a spray of small, high-velocity particles was launched at the beginning of 32 eruptions analyzed. If we extrapolate using the velocity versus size trend as plotted in red in Figure 9, we obtain

$$U = -120.2 \ln(D) + 504.93 \quad R^2 = 0.97 \tag{10}$$

over the size range of 0.2 cm to 60 cm. Assuming that the particles reach their terminal velocity in the conduit, the velocity of the gas cloud (U_{gas}) can be related to the velocity of the particles (U) by [*Steinberg and Babenko*, 1978]

$$U_{gas} = U + \left(\sqrt{\frac{4g\rho_{particle}}{3C_D\rho_{gas}}}\right)\sqrt{D} \tag{11}$$

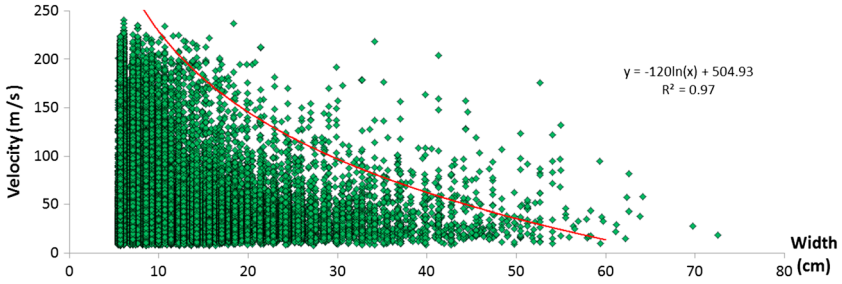

Figure 9. Correlation between size and velocity for particles detected in the whole data set (SWC 2012 and SWC/NEC in 2014).

where g is the acceleration due to gravity, $\rho_{particle}$ is the particle density, ρ_{gas} is the gas density, C_D is the drag coefficient, and D is the particle diameter. Following *Chouet et al.* [1974], this equation has commonly been reduced to [e.g., *Ripepe et al.*, 1993]

$$U = U_{gas} - k\sqrt{D} \tag{12}$$

The trend of equation (10) defines the maximum limit of the D versus U scatters for each of our 31 explosions. In our data this empirical fit can be approximated by

$$\mathrm{U} = \mathrm{U}_{gas} - \sqrt{D} \tag{13}$$

Thus, following *Steinberg and Babenko* [1978], the upper limit of the relation follows a rule whereby particle velocity decreases with the square root of particle diameter. Below this limit, we have a "black cloud" of data points (Figure 9). This scatter is likely due to the large number of gas densities likely apparent between eruptions and during single events [*Harris et al.*, 2012]. Our observations of both visible, thermal, and UV videos suggest that all of the parameters in *Steinberg and Babenko*'s [1978] relation, including gas density, likely change over the time scale of a few tenths of a second, making application of such a simple relation to a single explosion problematic to say the least. In addition, although some particles may be coupled to the gas phase, thereby obeying this law, others will be undergoing varying degrees of decoupling. Complete decoupling means that we revert to the relation

$$U = \sqrt{\frac{dg}{\sin(2\theta)}} \tag{14}$$

in which d is the distance reached by the particle and θ is the launch angle. In short, the black cloud in Figure 9 is formed because particles with the same width show a large range of velocity and vice versa. For the same particle size, we can have a large range of velocity and vice versa; the same velocity can be reached by different particles. This scatter indicates a large variability in the analyzed explosive dynamics. The trend becomes narrower toward the large particle-low velocity end of the plot, indicating that variability increases as particle size decreases, suggesting that only the smallest particles are capable of revealing the complexities and variability of particle launch dynamics.

Using equation (10), we obtain a maximum velocity of 456 m/s for a particle width of 1.5 cm, in line with the findings of *Taddeucci et al.* [2012a], and up to 700 m/s for the smallest particle to which this relation can be applied. Note that these "extrapolated" maximum velocities are based on projection from data for observed particles into a field of non-observed particles. However, the excellent correlation coefficient ($R^2 = 0.97$) for the trend gives us confidence in these extrapolated values for particles that were too small to be resolved by our camera system. For us, the extrapolations are thus only valid down to lower size range of lapilli and cannot be used to assess ash parameters. Following our argument above, our physical explanation for these high velocities is that of *Harris et al.* [2012], whereby the smallest particles are carried by the fast moving gas phase which accounts for the highest velocities found for the lapilli so that they are markers for the gas velocity. Bombs are decoupled from the gas phase due to their mass and are just driven by momentum so that lowest velocities are found for the largest particles.

4.3. Correlation With Seismic Amplitude

Seismoacoustic recordings collected during the explosions of the 2012 experiment were in general weak. No clear acoustic signals associated with the explosions could be identified at the reference station. This precluded assessment of thermo-infrasonic following *Ripepe et al.* [2001, 2002], seismic time delays, or assessment of free-surface level.

From a seismic point of view, signals related to explosions at Stromboli classically include a short-period (SP) waveform (1–5 Hz) [*Ripepe*, 1996], a high-frequency (HF) component (>5 Hz) corresponding to the coupling to the ground of the infrasonic wave [*Braun and Ripepe*, 1993], and a very long period component with periods up to several tens of seconds [*Neuberg et al.*, 1994]. During the 2012 experiment, SP signals were often barely above the levels of background tremor and HF acoustic phases were non identifiable. VLP signals were the most prominent feature associated with the explosions with the clearer waveforms being observed

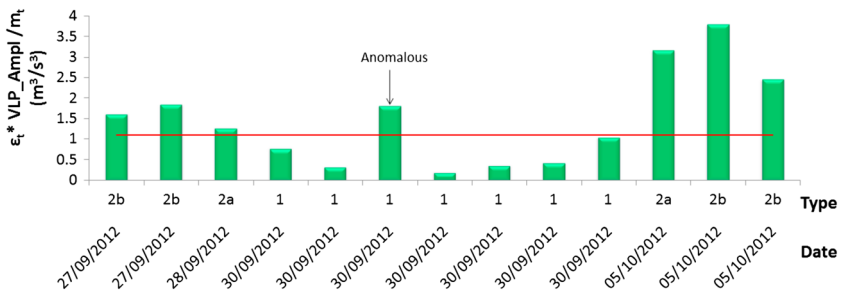

Figure 10. Volumetric acceleration of different types of eruption detected visually on the infrared video used for the 2012 data set.

on the east-west component nearly radial to the craters. We calculated the peak to peak amplitudes of these VLP components for the EW component after filtering between 0.03 and 0.2 Hz with a two-pole Butterworth causal filter. We find that the Type 1 events had the lowest seismic amplitudes, where some of them were so feeble that they were within the tremor noise. There is one exception, the sixth event in the series, which was particularly long, lasting 50 s; all other events being 5 to 22 s in duration. Type 2a and 2b events were generally associated with greater amplitudes. There is a weaker correlation with kinetic energy and mass, but if we combine all three parameters, we arrive at the trend of Figure 10. Given that these parameters provide the strongest relation, we suggest that they play a fundamental role in controlling the process or they are the main variables controlled by the process.

4.4. Source Mechanism

We see from Table 2 that during the 2012 experiment, the eruptions cycled from ash-and-bomb rich (Types 2a and 2b) to bomb-and-gas rich (Type 1) and back again to Types 2a and 2b over a time scale of 10 or so hours. We also find that during 2012, explosions had lower particle numbers, velocities, and kinetic energies than in 2014 but involved greater masses. This, as already stated, points to a more efficient, energetic, and gas-driven explosion mechanism in 2014 compared with 2012.

Eruptions at Stromboli have been classically explained by generation of a large gas mass, or slug, which ascends the magma-filled conduit to burst at the free surface [*Jaupart and Vergniolle*, 1989; *Vergniolle and Brandeis*, 1996; *James et al.*, 2004]. Bomb-rich eruptions may be the result of fragmentation of a viscous, degassed plug or rheological layer at the head of the magma column which fragments upon arrival of the slug [*Gurioli et al.*, 2014], and/or the extraction of the degassed material stuck to the conduit wall by passage of the slug [*Lautze and Houghton*, 2005]. Textures and associations of different textural facies, including the presence of dense, crystal-rich degassed material mixed with juvenile material in bombs sampled by *Gurioli et al.* [2014], were consistent with the cap model. Breaking of a cap would also require a greater degree of seismic energy, as opposed to a situation where fragmentation is caused by bursting of a bubble at a low viscosity and yield strength magma surface [*Gurioli et al.*, 2014; *Leduc et al.*, 2015]. It would also explain lower particle numbers, velocities, and kinetic energies, along with larger particles, during such cap-dominated events. We thus suggest that during Types 1 and 2 activity, which possess these dynamic characteristics, a complete cap was in place which fragmented upon arrival of the gas slug, following the model of *Gurioli et al.* [2014].

During Types 1 and 2 events, *Gurioli et al.* [2014] and *Leduc et al.* [2015] suggested that magma levels were relatively high with the magma column being capped by degassed material and/or, following *Patrick et al.* [2007], scoria. While fragmentation of the cap feeds an impressive Type 1 particle emission [*Gurioli et al.*, 2014], the particles being accidental incorporation of previously degassed material [*Harris et al.*, 2012], grinding of scoria adds the ash component to the Type 2 events [*Patrick et al.*, 2007]. However, convective overturn of the cap can result in a cleaner conduit, with a lower level, where the bubble bursts at a fresh magma surface, or through a thinner cap, so that the particle load of the gas jet is small-to-nonexistent, and exit velocities are high due to coupling of rare but small particles to the gas phase [*Leduc et al.*, 2015]. These are Type 0 events. We indeed find that the fastest moving particles are small but rare and are capable of attaining velocities toward 500 m/s. The fresh conduit scenario fits our Type 1 scenario for the 2012 data set, where seismic energy, kinetic energy, and particle mass are lower due to the presence of a smaller cap than during the Type 2a and 2b events (Figure 10). However, we do not record true Type 0 events as particle loads

are still quite high. In addition, the lower masses and smaller particle sizes, but high velocities, particle numbers, and kinetic energies during 2014 suggest a more efficient, less cap-dominated fragmentation model for 2014 compared with 2012. However, again, relatively high particle masses are inconsistent with true, completely cap-free and particle-free Type 0 activity.

There is bound to be a continuum of styles from Type 0 through Type 1 to Types 2a and 2b. We suggest, that the continuum is from Type 0, which has the lowest particle masses and no cap influence, through Type 1 —which has moderate particle masses and some cap influence—to Types 2a and 2b, which have highest particle masses and a strong cap influence and/or interaction with scoria plugs. As we move through this sequence, the gas influence also decreases so that the size of the population of fastest moving particle decreases, kinetic energy decreases, but seismic energy increases as more energy is produced by cap breakage than simple bubble bursting in a low-viscosity fluid. Fragmentation efficiency also decreases so that the number of particles erupted decreases, but their size increases. Between the two end-member conduit scenarios, capped and uncapped, there is a density-driven convective overturn event [*Allard et al.*, 1994; *Stevenson and Blake*, 1998], after which the cap rebuilds, to push the system back to the initial conditions. The duration of our cycles (~10 h) may be the time scale of cap construction and overturn during the 2012 experiment. Indeed, the time scale of the persistence of our two eruption types and associated characteristics recorded here is consistent with the time scale of convective overturn recorded in similar geophysical data sets at Stromboli [*Ripepe et al.*, 2002, 2005, 2008]. Convective overturn at Stromboli has been associated with changes in the seismic-acoustic-thermal delay [*Ripepe et al.*, 2001, 2002], which are thought to relate to changes in the magma level [*Ripepe et al.*, 2005, 2008]. Unfortunately, during our analysis period, seismic signals were so weak that we were unable to examine delay times.

5. Conclusions

We collected high frame rate thermal video for 31 normal explosions at Stromboli during October 2012 and May 2014. Constraint of the vent-leaving particle dynamics allowed us to move closer to validating a model for normal explosive activity at Stromboli, whereby the system cycles between periods of capped behavior during which the slug fragments through a cap of degassed magma and free-surface behavior when the cap is absent so that slugs burst through lower viscosity (uncapped) magma.

We first used the algorithm of *Bombrun et al.* [2014] to obtain a statistically robust database of 83,000 particles to compute the size, mass, and velocity of each particle. Statistically, the distribution for all parameters computed for the 13 eruptions of 2012 is similar to that obtained for the 18 eruptions of 2014. Most of the particles have sizes between 5 cm and 15 cm, and the majority of individual bomb masses are below 0.4 kg. However, although 4950 (6%) of the particles are heavier than 5 kg, they represent 59% of the total mass erupted.

The particle velocity distribution is positively skewed with a mode between 20 m/s and 30 m/s. Normal explosive activity at Stromboli has typically been viewed as involving large particles with relatively low velocities, with a mean of around 25 m/s [*Chouet et al.*, 1974; *Ripepe et al.*, 1993]. Recently, however, *Delle Donne and Ripepe* [2012] and *Harris et al.* [2012] have shown that a few small (typically lapilli sized) particles can be ejected as part of an initial high velocity gas jet, which has average velocities of 80 m/s and a maximum of 405 m/s [*Taddeucci et al.*, 2012a]. Our data support this duality. The spatial resolution of our system allows us to detect particles down to 5 cm. In our data, most (probably all) of the bombs (size greater than 6.4 cm) are detected, and the bomb velocity distribution has a mode between 20 m/s and 30 m/s. Our data also indicate that the smallest particles, carried by the gas jet, have the highest velocities with a maximum measured speed of 240 m/s, and a projected maximum potential velocity of 700 m/s for the smallest lapilli (0.2 cm in size), as extrapolated to the lowest particle size to which the relationship plotted in Figure 9 can be applied.

Patrick et al. [2007] and *Leduc et al.* [2015] classified normal explosions at Stromboli by visual clustering, the classification depending on whether they were ballistic dominated (Type 1), ash dominated, with (2a) or without (2b) particles, or gas dominated (Type 0). We used our measured parameters to cluster our explosions into the same four classes. The correlation with seismic data helps to understand the source mechanism and supports the models of *Gurioli et al.* [2014] and *Leduc et al.* [2015]: Types 2a and 2b events are a consequence of the presence of a viscous, degassed cap at the head of the magma column, its fragmentation providing 10^3 to 10^4 kg of solid material in each eruption. However, Type 1 is a consequence of slug bursting in a "cleaner" conduit, involving a lower mass of solid material, where true Type 0 eruptions involve almost no solid material.

Appendix A: Southwest 2012 Data Set

Reference	Number of Detected Particles	Duration	
		Number of Frames	Times (s)
09-27_154909271	1,788	2,692	13
09-27_155839983	3,064	1,600	8
09-28_135432903	715	1,000	5
09-30_125847157	3,015	2,352	12
09-30_131721017	975	3,698	18
09-30_132029052	4,215	9,999	50
09-30_133102430_1	648	3,300	16
09-30_133102430_2	1,255	2,485	12
09-30_134451828	5,240	4,513	23
09-30_135413067	4,382	3,376	17
10-05_144505552	1,392	2,502	13
10-05_145321701	1,558	2,215	11
10-05_150241747	1,305	2,963	15
All	29,552	3,284[a]	16[a]

[a]Mean value.

Reference	Width (cm)				
	Maximum	Minimum	Mean	Median Value	Standard Deviation
09-27_154909271	59	5.8	12	10	5.4
09-27_155839983	62	5.8	14	12	6.5
09-28_135432903	50	5.7	10	9	5.2
09-30_125847157	50	5.5	12	11	5.2
09-30_131721017	42	5.5	14	12	4.9
09-30_132029052	56	5.5	14	12	5.2
09-30_133102430_1	52	5.5	14	12	6.6
09-30_133102430_2	41	5.5	12	11	4.9
09-30_134451828	46	5.5	11	10	4.3
09-30_135413067	37	5.5	11	10	4.0
10-05_144505552	64	5.9	14	12	5.2
10-05_145321701	48	5.9	12	10	5.6
10-05_150241747	62	5.9	15	13	7.4
Mean	51	5.6	12	11	5.4

Reference	Velocity (m/s)				
	Maximum	Minimum	Mean	Median Value	Standard Deviation
09-27_154909271	224	8.3	37	27	29
09-27_155839983	218	8.4	34	27	23
09-28_135432903	199	8.4	35	25	29
09-30_125847157	198	8.0	33	25	24
09-30_131721017	158	8.9	24	20	15
09-30_132029052	195	8.1	29	24	18
09-30_133102430_1	203	9.0	22	19	18
09-30_133102430_2	180	8.4	27	22	18
09-30_134451828	204	7.7	32	24	23
09-30_135413067	216	8.2	34	27	23
10-05_144505552	221	9.3	41	35	29
10-05_145321701	209	8.5	41	30	32
10-05_150241747	223	8.5	34	26	27
Mean	204	8.4	33	25	24

	Mass (kg)					
Reference	Maximum	Minimum	Mean	Median Value	Standard Deviation	Total
09-27_154909271	158	0.2	2.2	0.8	6.4	3,900
09-27_155839983	185	0.2	3.4	1.4	8.1	10,377
09-28_135432903	81	0.2	1.8	0.6	6.1	1,270
09-30_125847157	110	0.2	2.0	0.9	4.8	6,137
09-30_131721017	58	0.2	2.8	1.5	4.5	2,698
09-30_132029052	142	0.2	2.8	1.5	5.8	11,822
09-30_133102430_1	108	0.2	3.8	1.5	10	2,489
09-30_133102430_2	60	0.2	1.9	0.9	3.9	2,360
09-30_134451828	71	0.2	1.4	0.7	3.1	7,261
09-30_135413067	32	0.2	1.2	0.7	2.2	5,449
10-05_144505552	214	0.2	4.5	1.6	6.1	6,224
10-05_145321701	101	0.2	2.2	0.9	5.5	3,467
10-05_150241747	135	0.2	4.6	1.6	11	5,949
Mean	112	0.2	2.7	1.1	6.0	5,339

Appendix B1: Southwest 2014 Data Set

		Duration	
Reference	Number of Detected Particles	Number of Frames	Times (s)
05-18_132733420	3,246	3,761	19
05-18_132801415	2,318	3,373	17
05-18_133328389	4,200	4,437	22
05-18_133918611	4,385	2,913	15
05-18_134008344	2,187	3,122	16
05-18_135314670	3,019	1,984	10
05-18_135359440	3,243	2,302	11
05-18_135801197	2,215	1,986	10
05-18_141207229	612	1,215	6.1
05-18_141608738	2,839	1,839	9.2
05-18_142529169	1,150	1,168	5.9
05-18_143354953	813	1,837	9.2
05-18_144559561	1,266	1,408	7.0
All	31,493	2,411[a]	12[a]

[a]Mean value.

	Width (cm)				
Reference	Maximum	Minimum	Mean	Median Value	Standard Deviation
05-18_132733420	50	5.7	7.7	5.7	4.5
05-18_132801415	53	5.7	7.9	5.7	4.6
05-18_133328389	58	5.7	7.5	5.7	4.4
05-18_133918611	63	5.7	7.4	5.7	4.3
05-18_134008344	53	5.7	8.1	5.7	5.1
05-18_135314670	54	5.7	7.3	5.7	3.8
05-18_135359440	70	5.7	7.3	5.7	4.3
05-18_135801197	58	5.7	8.0	5.7	5.3
05-18_141207229	54	5.7	9.9	5.7	7.7
05-18_141608738	54	5.7	7.4	5.7	3.8
05-18_142529169	54	5.7	8.8	5.7	6.3
05-18_143354953	73	5.7	12	7.1	10
05-18_144559561	55	5.7	8.5	5.7	6.1
Mean	58	5.7	8.3	5.8	5.4

	Velocity (m/s)				
Reference	Maximum	Minimum	Mean	Median Value	Standard Deviation
05-18_132733420	222	8.0	48	34	38
05-18_132801415	224	8.0	53	40	40
05-18_133328389	226	8.0	52	39	39
05-18_133918611	221	8.1	54	42	40
05-18_134008344	219	8.2	47	34	38
05-18_135314670	220	8.1	48	34	38
05-18_135359440	222	8.2	59	47	42
05-18_135801197	216	8.0	50	38	38
05-18_141207229	209	8.3	42	29	37
05-18_141608738	219	8.0	57	45	40
05-18_142529169	196	8.3	43	30	34
05-18_143354953	184	8.2	42	30	32
05-18_144559561	224	8.2	46	32	38
Mean	216	8.1	49	37	38

	Mass (kg)					
Reference	Maximum	Minimum	Mean	Median Value	Standard Deviation	Total
05-18_132733420	106	0.2	1.0	0.2	4.4	3,116
05-18_132801415	127	0.2	1.0	0.2	5.5	2,427
05-18_133328389	182	0.2	1.0	0.2	5.5	4,019
05-18_133918611	220	0.2	0.9	0.2	5.8	4,098
05-18_134008344	117	0.2	1.2	0.2	6.2	2,714
05-18_135314670	149	0.2	0.7	0.2	4.5	2,242
05-18_135359440	268	0.2	0.9	0.2	7.1	3,001
05-18_135801197	172	0.2	1.4	0.2	7.8	3,016
05-18_141207229	125	0.2	3.0	0.2	12	1,844
05-18_141608738	122	0.2	0.8	0.2	4.0	2,151
05-18_142529169	132	0.2	1.9	0.2	8.4	2,149
05-18_143354953	287	0.2	5.8	0.3	20	4,741
05-18_144559561	157	0.2	1.8	0.2	8.5	2,280
Mean	166	0.2	1.6	0.2	7.7	2,908

Appendix B2: Northeast 2014 Data Set

		Duration	
Reference	Number of Detected Particles	Number of Frames	Times (s)
05-17_172319583	5,021	1,737	8.7
05-17_180115473	3,952	1,535	7.7
05-17_182500440	5,316	3,232	16
05-17_185245215	5,304	2,175	11
05-17_193118327	2,582	1,494	7.5
All	22,175	2,035[a]	10[a]

[a]Mean value.

	Width (cm)				
Reference	Maximum	Minimum	Mean	Median Value	Standard Deviation
05-17_172319583	60	6.1	9.3	7.6	5.2
05-17_180115473	57	6.1	9.2	7.6	5.3
05-17_182500440	64	6.1	9.7	7.6	5.9
05-17_185245215	61	6.1	9.1	7.6	5.1
05-17_193118327	49	6.1	8.7	6.1	5.1
Mean	58	6.1	9.2	7.3	5.3

	Velocity (m/s)				
Reference	Maximum	Minimum	Mean	Median Value	Standard Deviation
05-17_172319583	240	9.4	56	42	40
05-17_180115473	232	8.7	52	39	38
05-17_182500440	237	8.8	49	35	37
05-17_185245215	237	8.6	53	40	39
05-17_193118327	234	8.7	54	40	40
Mean	235	8.7	52	38	39

	Mass (kg)					
Reference	Maximum	Minimum	Mean	Median Value	Standard Deviation	Total
05-17_172319583	194	0.2	1.5	0.3	5.9	7,554
05-17_180115473	148	0.2	1.5	0.3	6.3	6,003
05-17_182500440	223	0.2	1.9	0.3	7.6	10,255
05-17_185245215	215	0.2	1.4	0.3	5.9	7,586
05-17_193118327	84	0.2	1.4	0.2	5.3	3,542
Mean	168	0.2	1.6	0.3	6.3	6,846

Acknowledgments
We thank Jacopo Taddeucci, Loÿc Vanderkluysen, and Mike Poland for their helpful and constructive recommendations. We also thank Maurizio Ripepe for the seismic data and his productive comments. This research was financed by the French Government Laboratory of Excellence initiative n°115 ANR-10-LABX-0006, the Région Auvergne, and the European Regional. Data are available on demand. Please contact the corresponding author.

References

Allard, P., J. Carbonnelle, N. Metrich, H. Loyer, and P. Zettwoog (1994), Sulphur output and magma degassing budget of Stromboli volcano, *Nature*, *368*, 326–330, doi:10.1038/368326a0.

Bhattacharyya, A. (1943), On a measure of divergence between two statistical populations defined by their probability distributions, *Bull. Calcutta Math. Soc.*, *35*(1), 99–109.

Blackburn, E., L. Wilson, and R. Sparks (1976), Mechanisms and dynamics of strombolian activity, *J. Geol. Soc. Lond.*, *132*(4), 429–440.

Bombrun, M., V. Barra, and A. Harris (2014), Algorithm for particle detection and parameterization in high-frame-rate thermal video, *J. Appl. Remote Sens.*, *8*(1), 083549, doi:10.1117/1.JRS.8.083549.

Braun, T., and M. Ripepe (1993), Interaction of seismic and air waves recorded at Stromboli volcano, *Geophys. Res. Lett.*, *20*, 65–68, doi:10.1029/92GL02543.

Chouet, B., N. Hamisevicz, and T. R. McGetchin (1974), Photoballistics of volcanic jet activity at Stromboli, *J. Geophys. Res.*, *79*(32), 4961–4976, doi:10.1029/JB079i032p04961.

Colò, L. (2012), Study of vesiculation in basalt magma through volcanological, textural and geophysical analyses: The case study of Stomboli, PhD dissertation, Dep. of Earth Sci., Univ. Firenze, Florence, Italy.

Delle Donne, D., and M. Ripepe (2012), High-frame rate thermal imagery of Strombolian explosions: Implications for explosive and infrasonic source dynamics, *J. Geophys. Res.*, *117*, B09206, doi:10.1029/2011JB008987.

Gaudin, D., M. Moroni, J. Taddeucci, P. Scarlato, and L. Shindler (2014a), Pyroclast tracking velocimetry: A particle tracking velocimetry-based tool for the study of strombolian explosive eruptions, *J. Geophys. Res. Solid Earth*, *119*, 5369–5383, doi:10.1002/2014JB011095.

Gaudin, D., J. Taddeucci, P. Scarlato, M. Moroni, C. Freda, M. Gaeta, and D. M. Palladino (2014b), Pyroclast tracking velocimetry illuminates bomb ejection and explosion dynamics at Stromboli (Italy) and Yasur (Vanuatu) volcanoes, *J. Geophys. Res. Solid Earth*, *119*, 5384–5397, doi:10.1002/2014JB011096.

Genco, R., M. Ripepe, E. Marchetti, C. Bonadonna, and S. Biass (2014), Acoustic wavefield and Mach wave radiation of flashing arcs in Strombolian explosion measured by image luminance, *Geophys. Res. Lett.*, *41*, 7135–7142, doi:10.1002/2014GL061597.

Goto, A., M. Ripepe, and G. Lacanna (2014), Wideband acoustic records of explosive volcanic eruptions at Stromboli: New insights on the explosive process and the acoustic source, *Geophys. Res. Lett.*, *41*, 3851–3857, doi:10.1002/2014GL060143.

Gurioli, L., A. J. Harris, L. Colò, J. Bernard, M. Favalli, M. Ripepe, and D. Andronico (2013), Classification, landing distribution, and associated flight parameters for a bomb field emplaced during a single major explosion at Stromboli, Italy, *Geology*, *41*, 559–562, doi:10.1130/G33967.1.

Gurioli, L., L. Colò, A. Bollasina, A. J. Harris, A. Whittington, and M. Ripepe (2014), Dynamics of Strombolian explosions: Inferences from field and laboratory studies of erupted bombs from Stromboli volcano, *J. Geophys. Res. Solid Earth*, *119*, 319–345, doi:10.1002/2013JB010355.

Harris, A. J. L. (2013), *Thermal Remote Sensing of Active Volcanoes: A User's Manual*, Cambridge Univ. Press, Cambridge, U. K.

Harris, A. J. L., and M. Ripepe (2007), Synergy of multiple geophysical approaches to unravel explosive eruption conduit and source dynamics: A case study from Stromboli, *Chem. Erde*, *67*, 1–35.

Harris, A. J. L., M. Ripepe, and E. A. Hughes (2012), Detailed analysis of particle launch velocities, size distributions and gas densities during normal explosions at Stromboli, *J. Volcanol. Geotherm. Res.*, *231-232*, 109–131, doi:10.1016/j.jvolgeores.2012.02.012.

Harris, A., et al. (2013), Modern multispectral sensors help track explosive eruptions, *Eos Trans. AGU*, *94*, 321–322, doi:10.1002/2013EO370001.

Holst, G. C. (2000), *Common Sense Approach to Thermal Imaging*, JCD, Winter Park, Florida.

James, M. R., S. J. Lane, B. Chouet, and J. S. Gilbert (2004), Pressure changes associated with the ascent and bursting of gas slugs in liquid-filled vertical and inclined conduits, *J. Volcanol. Geotherm. Res.*, *129*, 61–82.

Jaupart, C., and S. Vergniolle (1989), The generation and collapse of a foam layer at the roof of a basaltic magma chamber, *J. Fluid Mech.*, *203*, 347–380.

Kilgour, G., V. Manville, F. Della Pasqua, A. Graettinger, K. A. Hodgson, and G. E. Jolly (2010), The 25 September 2007 eruption of Mount Ruapehu, New Zealand: Directed ballistics, sutseyan jets, and ice-slurry lahars, *J. Volcanol. Geotherm. Res.*, *191*, 1–14.

Lautze, N. C., and B. F. Houghton (2005), Physical mingling of the magma and complex eruption dynamics in the shallow conduit at Stromboli volcano, Italy, *Geology*, *33*, 425–428, doi:10.1130/G21325.1.
Leduc, L., L. Gurioli, A. Harris, L. Colò, and E. F. Rose-Koga (2015), Types and mechanisms of Strombolian explosions: Characterization of a gas-dominated explosion at Stromboli, *Bull. Volcanol.*, *77*, 8.
Lorenz, V. (1970), Some aspects of the eruption mechanism of the Big Hole Maar, central Oregon, *Geol. Soc. Am. Bull.*, *81*, 1823–1830.
Macdonald, G. A. (1972), *Volcanoes*, Prentice-Hall, Englewood Cliffs, N. J.
MacQueen, J. (1967), Some methods for classification and analysis of multivariate observations, in *Proceedings of the Fifth Berkeley Symposium on Mathematical Statistics and Probability, Volume 1: Statistics*, pp. 291–297, Univ. of California Press, Berkeley, Calif.
McGetchin, T. R., M. Settle, and B. A. Chouet (1974), Cinder cone growth modeled after Northeast Crater, Mount Etna, Sicily, *J. Geophys. Res.*, *79*(23), 3257–3272, doi:10.1029/JB079i023p03257.
McGimsey, R. G., D. J. Schneider, C. A. Neal, and A. L. Roach (1999), Use of FLIR observations during eruption response at two Alaskan volcanoes, *Eos Trans. AGU*, *80*, 1146.
Neuberg, J., R. Luckett, M. Ripepe, and T. Braun (1994), Highlights from a seismic broadband array on Stromboli volcano, *Geophys. Res. Lett.*, *21*, 749–752, doi:10.1029/94GL00377.
Newhall, C. G., and S. Self (1982), The volcanic explosivity index (VEI): An estimate of explosive magnitude for historical volcanism, *J. Geophys. Res.*, *87*(C2), 1231–1238, doi:10.1029/JC087iC02p01231.
Patrick, M. R., A. J. Harris, M. Ripepe, J. Dehn, D. A. Rothery, and S. Calvari (2007), Strombolian explosive styles and source conditions: Insights from thermal (FLIR) video, *Bull. Volcanol.*, *69*(7), 769–784, doi:10.1007/s00445-006-0107-0.
Ripepe, M. (1996), Evidence for gas influence on volcanic seismic signals at Stromboli, *J. Volcanol. Geotherm. Res.*, *70*, 221–233, doi:10.1016/0377-0273(95)00057-7.
Ripepe, M., M. Rossi, and G. Saccorotti (1993), Image processing of explosive activity at Stromboli, *J. Volcanol. Geotherm. Res.*, *54*(3–4), 335–351, doi:10.1016/0377-0273(93)90071-X.
Ripepe, M., S. Ciliberto, and M. Della Schiava (2001), Time constraints for modeling source dynamics of volcanic explosions at Stromboli, *J. Geophys. Res.*, *106*(B5), 8713–8727, doi:10.1029/2000JB900374.
Ripepe, M., A. J. L. Harris, and R. Carniel (2002), Thermal, seismic and infrasonic evidences of variable degassing rates at Stromboli volcano, *J. Volcanol. Geoth. Res.*, *118*, 285–297.
Ripepe, M., A. J. Harris, and E. Marchetti (2005), Coupled thermal oscillations in explosive activity at different craters of Stromboli volcano, *Geophys. Res. Lett.*, *32*, L17302, doi:10.1029/2005GL022711.
Ripepe, M., D. D. Donne, A. Harris, E. Marchetti, and G. Ulivieri (2008). Dynamics of Strombolian activity, *The Stromboli Volcano: An Integrated Study of the 2002-2003 Eruption*, 39-48.
Rosi, M., A. Bertagnini, and P. Landi (2000), Onset of the persistent activity at Stromboli volcano (Italy), *Bull. Volcanol.*, *62*(4–5), 294–300, doi:10.1007/s004450000098.
Self, S., J. Kienle, and J. Huot (1980), Ukinrek Maars, Alaska: II. Deposits and formation of the 1977 crater, *J. Volcanol. Geotherm. Res.*, *7*, 39–65, doi:10.1016/0377-0273(80)90019-0.
Shindler, L., M. Moroni, and A. Cenedese (2012), Using optical flow equation for particle detection and velocity prediction in particle tracking, *Appl. Math. Comput.*, *218*(17), 8684–8694, doi:10.1016/j.amc.2012.02.030.
Steinberg, G. S., and J. L. Babenko (1978), Gas velocity and density determination by filming gas discharges, *J. Volcanol. Geotherm. Res.*, *3*, 89–98.
Stevenson, D. S., and S. Blake (1998), Modeling the dynamics and thermodynamics of volcanic degassing, *Bull. Volcanol.*, *60*, 307–317, doi:10.1007/s004450050234.
Taddeucci, J., P. Scarlato, A. Capponi, E. Del Bello, C. Cimarelli, D. Palladino, and U. Kueppers (2012a). High-speed imaging of Strombolian explosions: The ejection velocity of pyroclasts, *Geophys. Res. Lett.*, *39*, L02301, doi:10.1029/2011GL050404.
Taddeucci, J., M. A. Alatorre-Ibargüengoitia, M. Moroni, L. Tornetta, A. Capponi, P. Scarlato, D. B. Dingwell, and D. De Rita (2012b), Physical parameterization of Strombolian eruptions via experimentally-validated modeling of high-speed observations, *Geophys. Res. Lett.*, *39*, L16306, doi:10.1029/201GL052772.
Turner, J. S. (1962), The "starting plume" in neutral surroundings, *J. Fluid Mech.*, *13*, 356–368, doi:10.1017/S0022112062000762.
Vanderkluysen, L., H. Andrew, K. Kelfoun, C. Bonadonna, and M. Ripepe (2012), Bombs behaving badly: Unexpected trajectories and cooling of volcanic projectiles. (Springer-Verlag, Éd.), *Bull. Volcanol.*, *74*(8), 1849–1858, doi:10.1007/s00445-012-0635-8.
Vergniolle, S., and G. Brandeis (1996), Strombolian explosions: A large bubble breaking the surface of a lava column as a source of sound, *J. Geophys. Res.*, *101*(B9), 20,433–20,447, doi:10.1029/96JB01178.
Walker, G. (1971), Grain-size characteristics of pyroclastic deposits, *J. Geol.*, *79*(6), 696–714.
Walker, G. P. (1973), Explosive volcanic eruptions: A new classification scheme, *Geol. Rundsch.*, *62*(2), 431–446.
Washington, H. S. (1917), Persistence of vents at Stromboli and its bearing on volcanic bearing, *Geol. Soc. Am. Bull.*, *28*, 249–278.
Wohletz, K., M. Sheridan, and W. Brown (1989), Particle size distributions and the sequential fragmentation/transport theory applied to volcanic ash, *J. Geophys. Res.*, *94*(B11), 15,703–15,721, doi:10.1029/JB094iB11p15703.

Erratum

In the originally published version of this article, two instances of text were incorrectly typeset. The errors have since been corrected, and this version may be considered the authoritative version of record.